



# Mantle seismic anisotropy beneath NE China and implications for the lithospheric delamination hypothesis beneath the southern Great Xing'an range



Haichao Chen<sup>a</sup>, Fenglin Niu<sup>a,b,\*</sup>, Masayuki Obayashi<sup>c</sup>, Stephen P. Grand<sup>d</sup>, Hitoshi Kawakatsu<sup>e</sup>, Y. John Chen<sup>f</sup>, Jieyuan Ning<sup>f</sup>, Satoru Tanaka<sup>c</sup>

<sup>a</sup> State Key Laboratory of Petroleum Resource and Prospecting, and Unconventional Natural Gas Institute, China University of Petroleum, Beijing, China

<sup>b</sup> Department of Earth Science, MS-126, Rice University, Houston, USA

<sup>c</sup> Department of Deep Earth Structure and Dynamics Research, Japan Agency for Marine-Earth Science and Technology, Yokosuka, Japan

<sup>d</sup> Department of Geological Sciences, University of Texas at Austin, Austin, USA

<sup>e</sup> Earthquake Research Institute, The University of Tokyo, Tokyo, Japan

<sup>f</sup> Institute of Theoretical and Applied Geophysics, Peking University, Beijing, China

## ARTICLE INFO

### Article history:

Received 13 November 2016

Received in revised form 14 April 2017

Accepted 16 April 2017

Available online 17 May 2017

Editor: P. Shearer

### Keywords:

NE China

seismic anisotropy

lithosphere deformation

mantle flow

and delamination

## ABSTRACT

We measured shear wave splitting from SKS data recorded by the transcontinental NECESSArray in NE China to constrain lithosphere deformation and sublithospheric flows beneath the area. We selected several hundreds of high quality SKS/SKKS waveforms from 32 teleseismic earthquakes occurring between 09/01/2009 and 08/31/2011 recorded by 125 broadband stations. These stations cover a variety of tectonic terranes, including the Songliao basin, the Changbaishan mountain range and Zhangguanai range in the east, the Great Xing'an range in the west and the Yanshan orogenic belt in the southwest. We assumed each station is underlain by a single anisotropic layer and employed a signal-to-noise ratio (SNR) weighted multi-event stacking method to estimate the two splitting parameters (the fast polarization direction  $\phi$ , and delay time,  $\delta t$ ) that gives the best fit to all the SKS/SKKS waveforms recorded at each station. Overall, the measured fast polarization direction lies more or less along the NW–SE direction, which significantly differs from the absolute plate motion direction, but is roughly consistent with the regional extension direction. This suggests that lithosphere deformation is likely the general cause of the observed seismic anisotropy. The most complicated anisotropic structure is observed beneath the southern Great Xing'an range and southwest Songliao basin. The observed large variations in splitting parameters and the seismic tomographic images of the area are consistent with ongoing lithospheric delamination beneath this region.

© 2017 Elsevier B.V. All rights reserved.

## 1. Introduction

Northeast (NE) China lies between Korea and Mongolia, and is situated partly on the Sino-Korean craton and partly on the Inner Mongolia foldbelt (Fig. 1). Late Jurassic and Cretaceous volcanic rocks are widely distributed in the area with the age of rocks becoming younger towards the east, suggesting a west-to-east migration in magmatism (e.g., Wang et al., 2006; Zhang et al., 2010). The cause for this eastward volcanic migration is, however, still debated. For example, Wang et al. (2006) proposed a lithospheric delamination event, which was triggered by the collision of NE

\* Corresponding author at: Department of Earth Science, MS-126, Rice University, Houston, USA.

E-mail address: niu@rice.edu (F. Niu).

China and Siberia after the closure of the Mongol–Okhotsk ocean around ~160 Ma and then propagated progressively from west to east. The authors suggested that the thickening of the lithosphere is likely driven by the Mongol–Okhotsk subduction from the north-west and the initial stage of the collision. Zhang et al. (2010), on the other hand, believed that the lithospheric delamination is triggered by a flat-to-normal subduction change of the Paleo-Pacific plate beneath the east side of the area in the late Jurassic. These two geodynamic scenarios are expected to produce different fabric structures within the lithosphere, which can be mapped by seismic anisotropy (Silver, 1996).

Volcanism in NE China continued in the Cenozoic, but occurred much less extensively and in a rather episodic way (Liu et al., 2001). The volcanism was initiated at ~86 Ma and was mainly concentrated within the Songliao basin. At around 28 Ma, the vol-

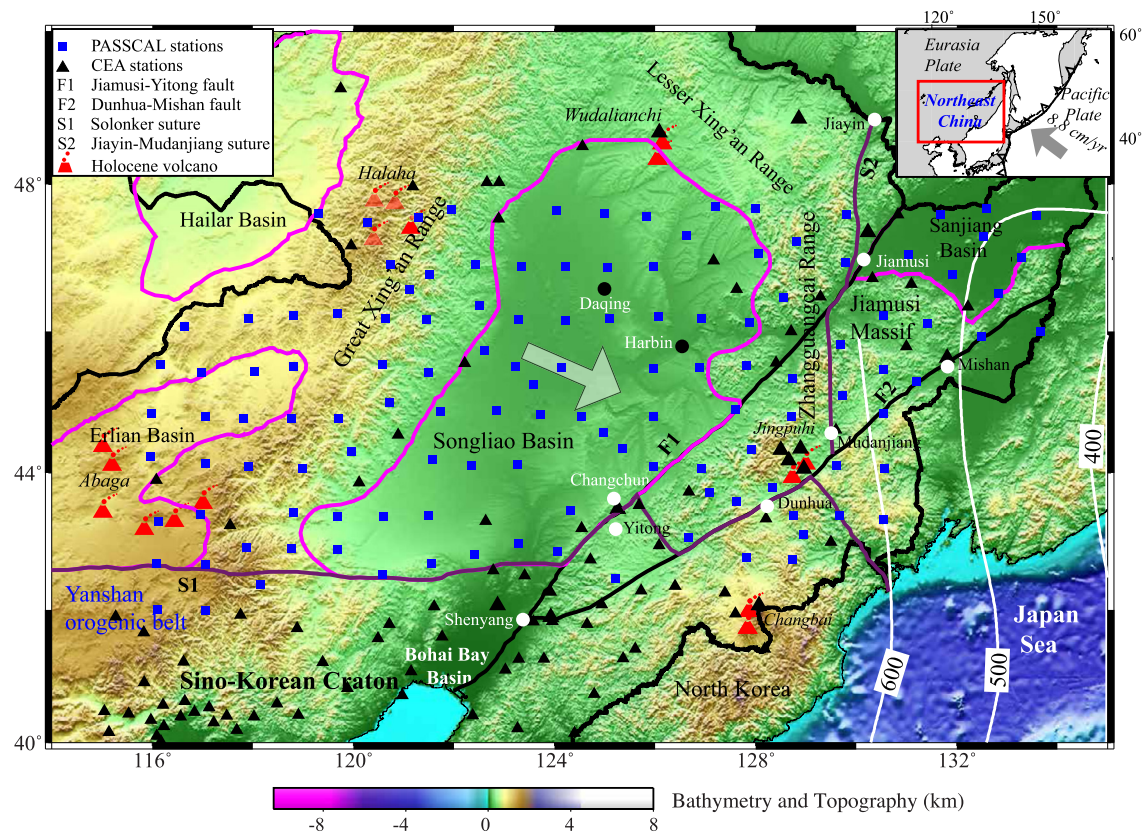


**Fig. 1.** Map showing topography, major faults, and tectonic units of northeast China. Blue solid squares and black solid triangles represent the 127 temporary and 108 permanent broadband stations of the NECESSArray, respectively. The temporary PASSCAL/ERI stations were deployed under an international collaboration between September of 2009 and August of 2011. The permanent stations are part of provincial seismic networks operated by the China Earthquake Administration (CEA). The array covers an area of 116°–134° east and 40°–48° north, roughly ~1800 km and ~800 km in the EW and NS direction, respectively. Red volcanic symbols show the five magmatic centers in the area, Changbaishan, Jingpohu, Wudalianchi, Halaha, and Abaga volcanic complexes. Solid white circles indicate major cities in the area. Pink lines outline the four major basins of the area: Songliao, Erlian, Hailar, and Sanjiang basins. F1 and F2 indicate the two major Quaternary faults; S1 and S2 are the two sutures in the area. The white arrow indicates the absolute plate motion with a velocity of ~2.6 mm/yr relative to hotspot frame based on the SKS-MORVEL (Zheng et al., 2014). The upper right inset shows the motion of the Pacific plate relative to the Eurasia plate. (For interpretation of the references to color in this figure legend, the reader is referred to the web version of this article.)

canism started to migrate towards the surroundings of the basin, in particular the eastern and western flanks (Liu et al., 2001), for example, the well-known Changbaishan and the Jingpohu volcanic complexes in the east and the Abaga and Halaha volcanoes in the west. Both shallow and deep processes have been invoked to explain the observed Cenozoic magmatism. One suggestion of a shallow mantle origin is edge driven convection along the boundaries of the Songliao basin (Niu, 2005), while many other models involve deep mantle upwelling associated with the subducting Pacific plate (e.g., Lei and Zhao, 2005; Zou et al., 2008; Xu et al., 2012; Tang et al., 2014), which reaches to ~600 km depth near the eastern edge of NE China. Mapping lateral variations of mantle flow beneath NE China thus has the potential to decipher the origin of the Cenozoic magmatism in the area.

Seismic anisotropy refers to velocity variations as a function of both propagation and polarization directions of seismic waves, which are known as propagation and polarization anisotropy, respectively. Polarization anisotropy is usually described by two parameters: the polarization direction of the fast shear wave,  $\varphi$ , and the delay time between the fast and slow waves,  $\delta t$ . The two parameters can be estimated from splitting or birefringence of shear waves, such as S, ScS and SKS phases, recorded at either local or teleseismic distances (e.g., Crampin, 1987; Silver and Chan, 1991).

Seismic anisotropy in the mantle is generally believed to be caused by preferred alignment of anisotropic minerals in response to mantle deformation. Magnesium-rich olivines are the most abundant constituent of the Earth's upper mantle, and possess a

highly anisotropic crystal structure, with up to 25% variation in P- and S-wave velocities. If the anisotropic minerals are preferentially aligned by a geodynamic process, their aggregates can produce a bulk anisotropy, i.e., seismic anisotropy. The amplitude of seismic anisotropy is generally in the order of a few percent because the crystals are only partially aligned (e.g. Silver, 1996). Consequently, seismic anisotropy can be used to constrain the processes that lead to deformation within the lithosphere and/or the underlying asthenosphere if deformation induced mineral alignment is well calibrated in lab (e.g., Mainprice et al., 2000).

A long-standing problem in global tectonics is how to estimate the absolute plate motions (APM) (Zheng et al., 2014), which are usually estimated with hotspot data (e.g., Morgan, 1972; Gripp and Gordon, 2002). The averaged APM of NE China calculated from the HS3-NUVELIA model (Gripp and Gordon, 2002) is approximately along the N67W direction with an annual velocity of ~2 cm/yr. Recently, an alternative method with shear wave splitting data has been proposed for estimating APM (e.g., Becker, 2008; Kreemer, 2009; Zheng et al., 2014). Since mantle seismic anisotropy is closely related to the preferred alignments of mantle minerals in response to asthenospheric flow, it is, in principle, possible to constrain the absolute plate motions with shear wave splitting data. Kreemer (2009) and Zheng et al. (2014) compiled a global shear wave splitting dataset with 474 fast polarization directions and obtained a global APM model, SKS-MORVEL. The predicted APM of NE China by the SKS-MORVEL is along ~N117E with a much smaller velocity, ~0.26 cm/yr. We found that the splitting

dataset used in constraining the SKS-MORVEL model has no coverage in China. This might explain the large discrepancy in the calculated APM of NE China between the two models. Thus determining seismic anisotropy beneath NE China is also of great significance in constraining the absolute motion of the Eurasia plate.

Li and Niu (2010) measured mantle seismic anisotropy beneath NE China using SKS/SKKS waveform data recorded by regional seismic networks of the China Earthquake Administration (CEA). They found significant variations in both the fast polarization direction and splitting time across the area. Both lithosphere deformation and asthenospheric flow appear to have contributed to the observed seismic anisotropy. It is noteworthy that station distribution of the CEA regional networks is highly non-uniform (black triangles in Fig. 1). There are very few stations inside the Songliao basin and the Great Xing'an range, which makes it difficult to map out the lateral variations of the anisotropic structures and further to link them with the magmatism in the area, especially within the Songliao basin and the Great Xing'an range.

This study is part of the international collaborative project, NECESSArray (the NorthEast China Extended Seismic Array), which deployed a total of 127 portable broadband seismographs in NE China to create a transcontinental array that evenly covers most of the NE China. The goal of the project is to build high-resolution seismic images of the crust and mantle beneath NE China to better constrain the subduction geometry of the Pacific plate and to better understand the large-scale extension and widespread magmatism in the area. In particular, we employed a signal-to-noise ratio (SNR) weighted multi-event stacking method to measure seismic anisotropy beneath the seismic array. Our goal is to characterize the relationships between plate motions, to constrain the style of regional extension, and to understand the magmatism of the area. Results are consistent with previous studies but also provide new constraints on an ongoing lithospheric delamination beneath the southern Great Xing'an range.

## 2. Data and analysis

We used the waveform data recorded by the NECESSArray, which consists of 127 temporary stations (blue squares) that were deployed under an international collaboration in NE China between September of 2009 and August of 2011. Station information can be found in the supplementary material of Tao et al. (2014). We also included shear-wave splitting measurements from 108 permanent stations of Li and Niu (2010) of 6 CEA regional seismic networks in the study area (Zheng et al., 2009). The permanent regional stations and the NECESSArray temporary stations form a large-scale array that evenly covers the area bounded by 116°–134° east and 40°–48° north, roughly 1800 km and 800 km in the E–W and N–S direction, respectively (Fig. 1).

We visually examined all the SKS/SKKS waveform data from earthquakes with a magnitude greater than  $M_w$  5.7, and an epicentral distance between 85° and 120° to the NECESSArray stations. We chose a total of 32 earthquakes that were well recorded by the array during its two-year deployment. The origin time and hypocentral information of the 32 events are listed in Table S1. Among the 32 earthquakes, 30 are located in the Tonga subduction zone. One earthquake is from Central America, and another one is the deep Spain earthquake that occurred on April 11 of 2010. The back azimuthal directions from these three locations are roughly perpendicular or parallel to each other (Fig. 2).

Actual orientation of the two horizontal components with respect to geographic north is of great importance to accurately measure the particle motion of the SKS/SKKS arrival and the fast polarization direction. Niu and Li (2011) proposed a method, which utilizes the particle motion of teleseismic P waves in the period

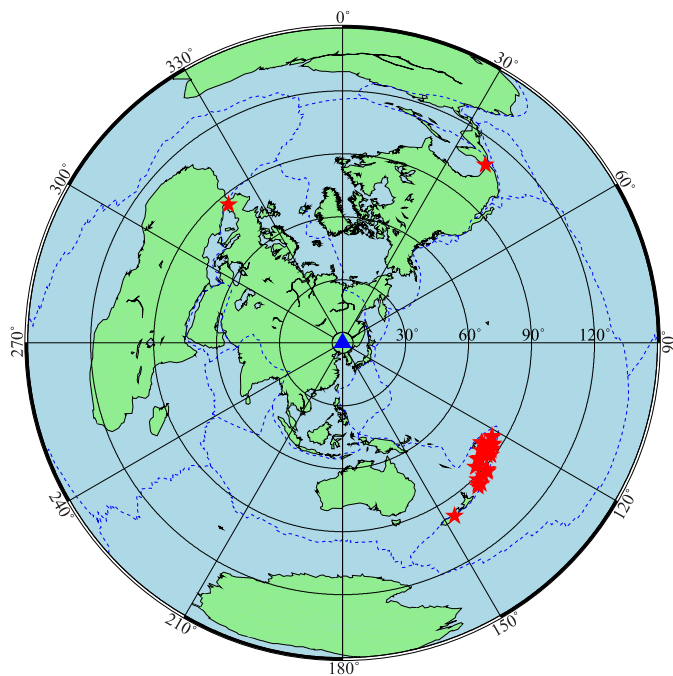


Fig. 2. Distribution of the 32 earthquakes (red stars) used in this study. The blue triangle indicates the center of the seismic array. 30 earthquakes are located in the Tonga subduction zone. (For interpretation of the references to color in this figure legend, the reader is referred to the web version of this article.)

band of 5 to 50 s, to constrain the sensor orientation of the two horizontal components. We applied this technique to the teleseismic P wavefield recorded by the NECESSArray stations and found that all the stations were properly aligned within  $\pm 10^\circ$ . For all the SKS/SKKS waveform data, we applied a bandpass filter of 0.04–0.5 Hz before measuring the fast polarization direction and splitting time. Fig. 3 shows an example of the recorded SKS arrival, which is clearly observed not only on the radial component (Fig. 3a), but also on the transverse component (Fig. 3b).

Due to the poor back azimuthal distribution of the 32 earthquakes, it is impossible to obtain the full azimuthal variations of the fast polarization direction and the splitting time, which are essential to distinguish whether seismic anisotropy beneath each station varies with depth or not. Li and Niu (2010) measured SKS/SKKS splitting of CEA stations in the area and found no apparent azimuthal variation of the splitting parameters at most of the stations. We thus assumed that each station is underlain by a simple depth-independent anisotropic medium, which allows us to use one set of splitting parameters ( $\varphi$ ,  $\delta t$ ) to fit all the SKS/SKKS waveforms recorded at the station.

We adopted a stacking technique developed by Li and Niu (2010) and Masy et al. (2011) to obtain the splitting parameters ( $\varphi$ ,  $\delta t$ ) at each station from multiple SKS/SKKS waveforms. Here we briefly review this method, which searches for a pair of  $\varphi$  and  $\delta t$  that minimizes either the summed energy of the transverse component

$$E_T(\varphi, \delta t) = \left( \sum_{i=1}^N w_i E_{Ti}(\varphi, \delta t) \right) / \sum_{i=1}^N w_i, \quad (1)$$

or the summed second eigenvalue  $\lambda_2$  of the covariance matrix of the corrected particle motion of all the SKS/SKKS data collected at one station

$$\Lambda_2(\varphi, \delta t) = \left( \sum_{i=1}^N w_i \lambda_{2i}(\varphi, \delta t) \right) / \sum_{i=1}^N w_i. \quad (2)$$

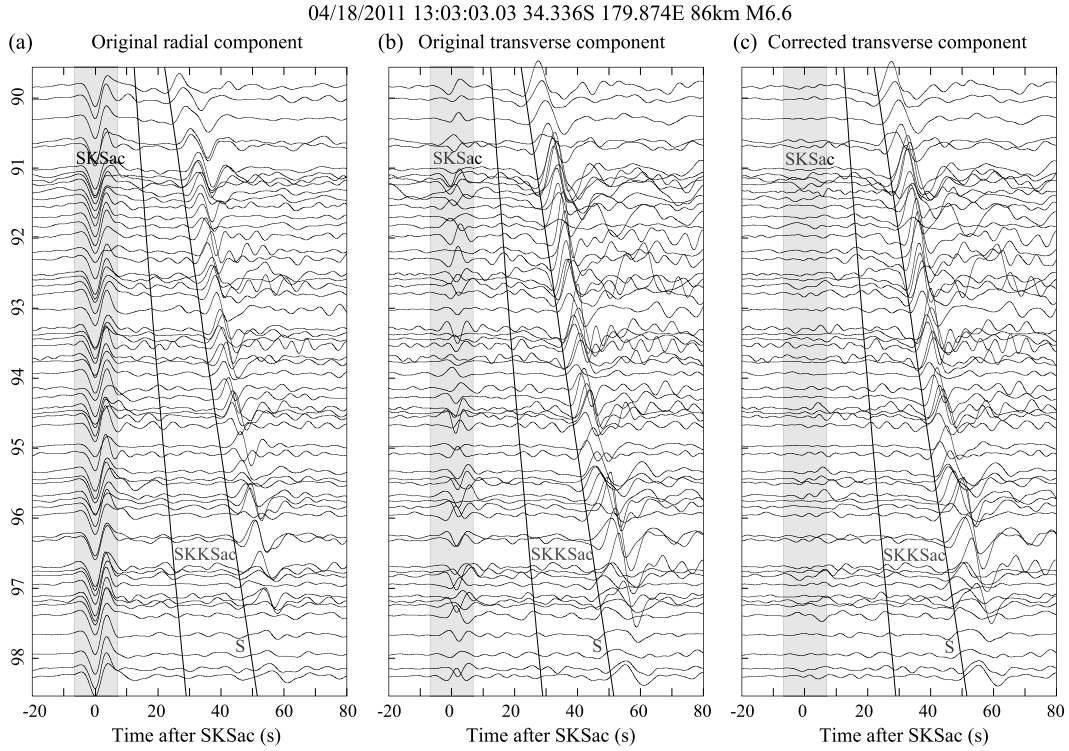


**Fig. 3.** An example of the SKS/SKKS waveforms on the radial (a) and transverse (b) components of the NECESSArray recordings from an intermediate depth earthquake occurring at the Tonga subduction zone. Only part of the stations are shown here for display purpose only. Note the significant SKS energy on the transverse component, indicative of the presence of seismic anisotropy beneath the stations. (c) Transverse components after being corrected by the measured seismic anisotropy.

Here  $E_{Ti}(\varphi, \delta t)$  and  $\lambda_{2i}(\varphi, \delta t)$  are, respectively, the transverse energy and the minor eigenvalue of the two-dimensional covariance matrix of the  $i$ th event, computed after correcting wave propagation effects in an anisotropic medium with a fast polarization direction of  $\varphi$  and delay time of  $\delta t$ .  $w_i$  is the weight of the  $i$ th event and is taken as the averaged SNR of the two horizontal components, and  $N$  is the total number of the events. To compute the SNR, we chose a noise time window before the SKS/SKKS arrival with the same length as the SKS/SKKS signal. We also used the total SKS/SKKS energy recorded at the two horizontal components to normalize the traces before computing the transverse energy  $E_{Ti}(\varphi, \delta t)$  to ensure that each event has the same contribution to the total energy. We varied  $\varphi$  in the range of  $0^\circ$  to  $180^\circ$  with an increment of  $1^\circ$ , and  $\delta t$  from 1.0 to 4.0 s in increments of 0.05 s. With the measured  $(\varphi, \delta t)$ , we further computed the polarization directions of the SKS/SKKS arrivals to make sure that they are consistent with the geometric back azimuths.

We also used the method of Li and Niu (2010) to compute errors in measuring the splitting parameters  $(\varphi, \delta t)$ :

$$\frac{E_T(\varphi, \delta t)}{E_T^{noise}} \leq 1 + \frac{k}{n-k} f_{k, n-k}(1-\alpha) \quad (3)$$

Here  $n$  is the number of degrees of freedom, which was calculated based on the empirical method of Silver and Chan (1991), i.e., 1 degree per second.  $\alpha$  is the confidence level,  $k=2$  is the number of parameters, and  $f$  represents the F-distribution.  $E_T^{noise}$  is the noise energy and was calculated by averaging the noise levels of the two horizontal components.

Examples of the summed transverse energy  $E_T(\varphi, \delta t)$  and the summed second eigenvalue  $\Lambda_2(\varphi, \delta t)$  at station YP.NE81 computed from 10 earthquakes with 3 different back azimuths are shown in Fig. 4a and 4b, respectively. The fast polarization direction ( $\varphi$ ) and

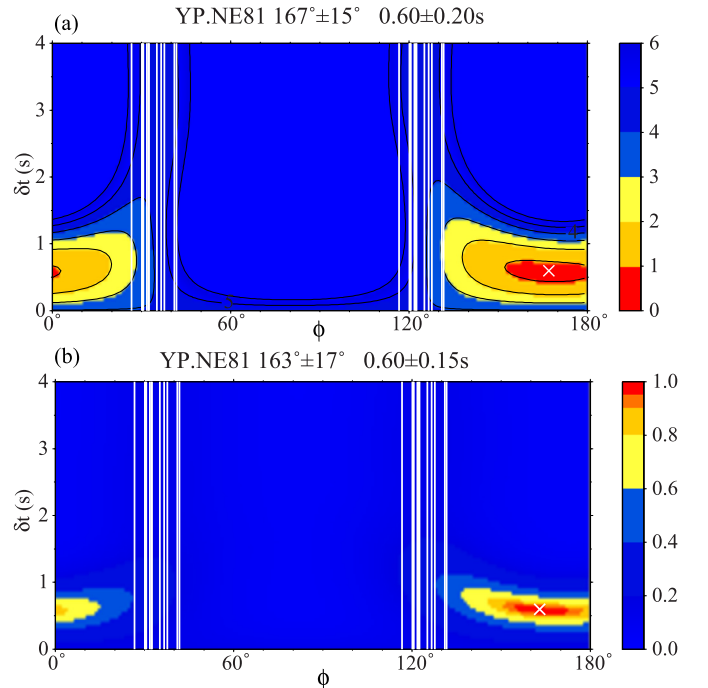


**Fig. 4.** An example of estimating the splitting parameters  $(\varphi, \delta t)$  at station YP.NE81. Color contour plot of  $E_T(\varphi, \delta t)$  (a) and  $\Lambda_2(\varphi, \delta t)$  (b) used in estimating the optimum  $(\varphi, \delta t)$ . White cross and red area represent the minimum value and the 95% confidence region, respectively. Vertical white lines indicate the polarization directions of the incoming SKS/SKKS waves and its perpendicular directions. Color scales used in plotting the contours are shown in the right side of the plots. (For interpretation of the references to color in this figure legend, the reader is referred to the web version of this article.)

the delay time ( $\delta t$ ) obtained from minimizing  $E_{Tmin}$  and  $\Lambda_{2min}$  are ( $167 \pm 15^\circ$ ,  $0.60 \pm 0.20$  s) and ( $163 \pm 17^\circ$ ,  $0.60 \pm 0.15$  s), which agree well with each other.

### 3. Results and discussion

We could not find good data at the YP.NE8H and YP.NEAD, so they were ignored. For the other stations we applied the stacking method and obtained the splitting parameters from all of them. Nearly half of the stations have less than 5 SKS waveforms. As mentioned above, the back azimuthal coverage of the selected events is rather poor, and a lot of the measurements are derived from a single back azimuth, therefore the estimated values could be the apparent splitting parameters of rather complicated anisotropic structures beneath the stations (e.g., Rumpker and Silver, 1998). Overall, the estimated parameters provide a reasonable fit to the SKS waveform splitting. The corrected SKS waveforms show little to no energy on the transverse component (Fig. 3c).

The measured splitting parameters at the 125 stations are listed in Table S2. The values shown here are estimated from the minimization of the second eigenvalue, i.e., the best linearity, which agree well with those derived from minimizing the transverse energy.

#### 3.1. NULL determination

Most of the SKS waveforms are from earthquakes in the Tonga subduction zone, which have a backazimuthal direction close to the fast or slow polarization directions, resulting in null measurements (Wustefeld and Bokelmann, 2007) that have no constraint on the splitting time. 65 stations are identified to have a null measurement (Table S2). It is important to determine that the absence or very weak SKS observed on the transverse component is due to weak seismic anisotropy or caused by the null direction. Wustefeld and Bokelmann (2007) proposed a novel technique to constrain null measurements by using the characteristic difference in the splitting parameters measured with the rotation correlation method and the minimum energy method. Here we suggest to utilize the frequency characteristics of SKS recorded on the transverse component to diagnose null measurements and isotropic observations. Silver and Chan (1988) showed that the radial and transverse components  $u_R(t)$  and  $u_T(t)$  are related to the source waveform  $s(t)$  by the following two equations:

$$\begin{aligned} u_R(t) &= s \left[ t - \left( t_0 - \frac{1}{2} \delta t \right) \right] \cos^2 \phi + s \left[ t - \left( t_0 + \frac{1}{2} \delta t \right) \right] \sin^2 \phi \\ u_T(t) &= \left\{ s \left[ t - \left( t_0 - \frac{1}{2} \delta t \right) \right] - s \left[ t - \left( t_0 + \frac{1}{2} \delta t \right) \right] \right\} \sin \phi \cos \phi \end{aligned} \quad (4)$$

Here  $\phi$  is the angle between the fast and radial directions, and  $t_0$  is the isotropic travel time. For null measurements,  $\phi$  is small, and when  $\delta t$  is small compared to the dominant period of  $s(t)$ , then equation (4) can be approximate by:

$$\begin{aligned} u_R(t) &\approx s \left[ t - \left( t_0 - \frac{1}{2} \delta t \right) \right] \cos^2 \phi \\ u_T(t) &\approx \frac{1}{2} s' (t - t_0) \delta t \sin 2\phi \end{aligned} \quad (4')$$

Thus, the transverse component,  $u_T(t)$ , is approximately proportional to the time derivative of the radial component,  $u_R(t)$ , which means the amplitude of SKS on the transverse component is expected to increase with increasing frequency content. Fig. 5 shows two examples of the SKS waveforms recorded at YP.NE41. The waveforms are filtered in 5 frequency/period bands: 1–10 s, 2–20 s, 3–30 s, 4–40 s, and 5–50 s, 2–20 s,

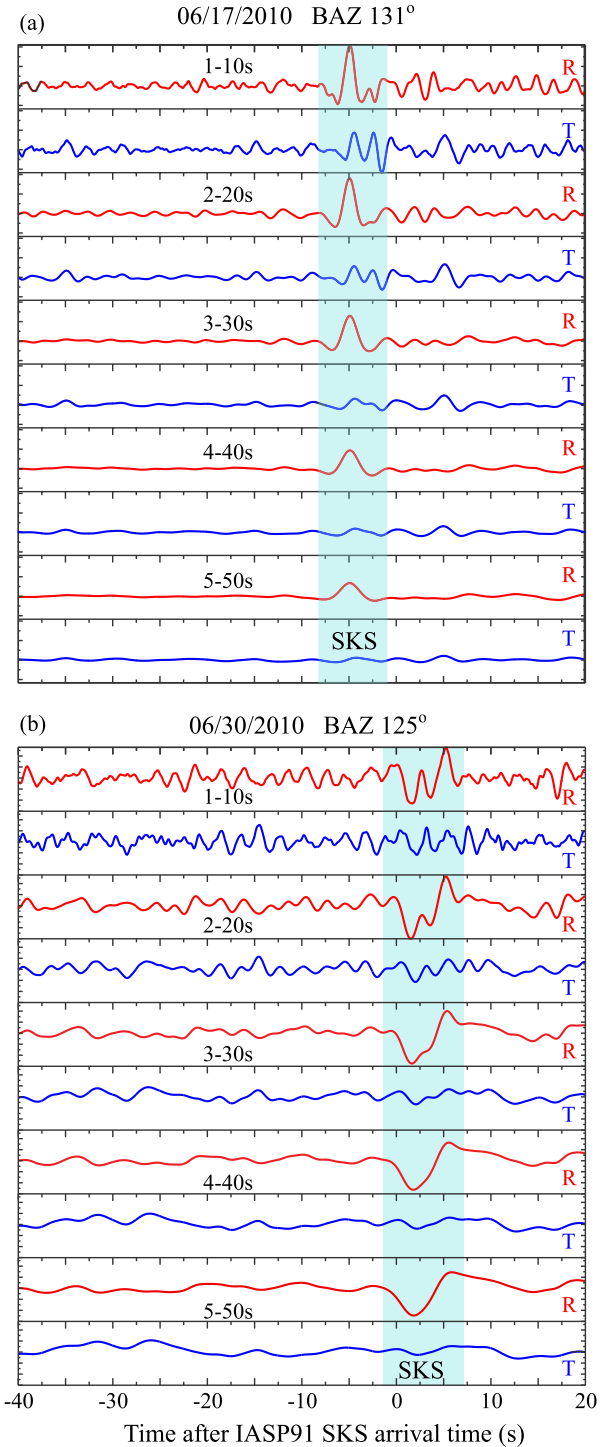


**Fig. 5.** SKS waveforms of the two Tonga earthquakes, 06/17/2010 (a) and 06/30/2010 (b), recorded at the station YP.NE41. The waveforms are filtered at 5 different frequency/period bands from the top to the bottom: 1–10 s, 2–20 s, 3–30 s, 4–40 s, and 5–50 s. The radial and transverse records are shown in red and blue, respectively. The back azimuth of the 06/17/2010 event is  $131^\circ$ , about  $7^\circ$  off the null direction ( $124^\circ$ ). The SKS can be clearly seen on the two short period bands 1–10 s and 2–20 s, suggesting the presence of seismic anisotropy beneath the station (a). The back azimuth of the 06/30/2010 event is aligned with the null direction, and no observable SKS is present on the transverse component (b). (For interpretation of the references to color in this figure legend, the reader is referred to the web version of this article.)

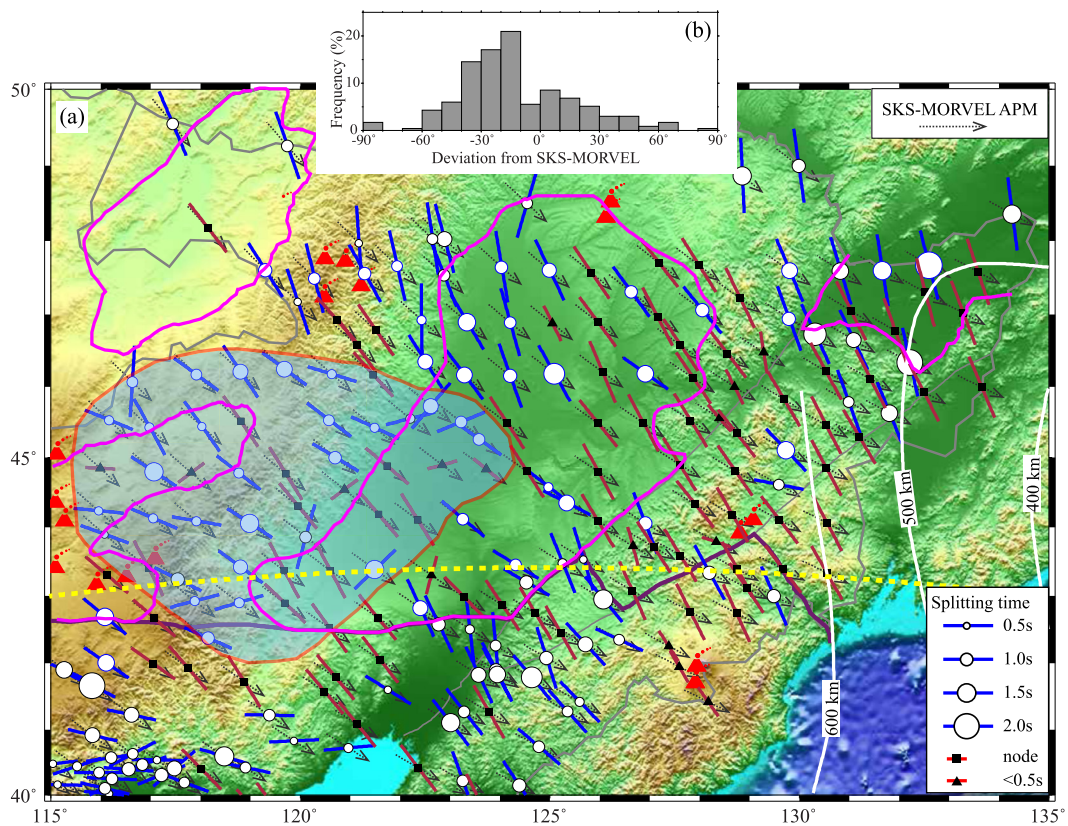


**Fig. 6.** (a) Measured splitting parameters are shown together with the topography of the study region. The solid blue lines and the white circles represent the measured fast polarization directions and splitting times ( $\geq 0.5$  s), respectively. The circles are scaled to splitting time values. Stations with a weak seismic anisotropy ( $\delta t < 0.5$  s) are indicated by solid black triangles. Black squares show node measurements with fast polarization directions being parallel or perpendicular to the arriving directions of the SKS/SKKS waves. Shaded area indicates the anomalous region with scattered fast polarization directions and splitting times. The dashed line plotted at each station represents the APM calculated from the SKS-MORVEL model (Zheng et al., 2014). The yellow dashed lines indicates the geographic location of schematic depth section shown in Fig. 8e. (b) Histogram shows the deviation of the observed fast polarization direction from the APM. (For interpretation of the references to color in this figure legend, the reader is referred to the web version of this article.)

3–30 s, 4–40 s, and 5–50 s. The 06/17/2010 event has a back azimuth of  $131^\circ$ ,  $\sim 7^\circ$  away from the measured null direction ( $124^\circ$ ). We can see significant SKS energy on the transverse component in the short-period band 1–10 s, and noticeable SKS amplitude in the next period band 2–20 s (Fig. 5a). On the other hand, SKS from the 06/30/2010 event is close to the null direction, and SKS is absent on the transverse component at all the frequency bands. For all the 65 stations with a null measurement, we conducted this frequency-amplitude analysis, and were able to confirm that 64 of the stations belong to true null measurements.

### 3.2. Lateral variations of the observed seismic anisotropy

Among the other 60 stations, the measured splitting time varies from 0.35 to 1.75 s, with an average of 0.84 s, slightly smaller than the global average (Silver, 1996). Fig. 6a shows the fast polarization directions and splitting times measured at the 125 NECESSArray stations, together with the measurements of the 108 permanent stations from Li and Niu (2010). Most stations show a NW–SE fast polarization direction, parallel to the regional extension direction. For comparison, we also show the APM directions of the SKS-MORVEL (Zheng et al., 2014), which estimates the rotation pole of the Amur plate to be ( $62.8^\circ\text{N}$ ,  $146.2^\circ\text{E}$ ) with an angular velocity of  $0.0595^\circ/\text{Ma}$ . The predicted APM varies from  $109^\circ$  to  $134^\circ$  with an average of  $117^\circ$ , while most of the measured fast polarization directions are roughly in the NW–SE direction, resulting in  $\sim 25^\circ$  discrepancy on average between the two directions (Fig. 6b). The deviation from the APM direction spreads across the whole area,

suggesting that the observed seismic anisotropy is unlikely to be caused by asthenospheric flow induced by the APM. Furthermore, we also notice that the APM of the Amur plate is not significantly different from zero in the SKS-MORVEL (Zheng et al., 2014), the AMP induced shear to the asthenosphere is thus expected to be very limited. Accordingly, we need to explore a variety of other mechanisms including lithosphere deformation and mantle flows associated with other mantle processes for the causes of the observed seismic anisotropy.

In order to characterize the lateral variations of the observed seismic anisotropy across the study area as well as their underlying physical mechanisms, we averaged the fast polarization direction and splitting time using circular caps with a radius of  $1^\circ$  (Figs. 7a and 7b), which is roughly the lateral extent of the SKS wave in the upper mantle. As mentioned above, the NW–SE fast polarization direction is predominant in the study area except for the southeastern part (Figs. 7a and 7c). Li and Niu (2010) argued that the observed seismic anisotropy is likely to reflect the “frozen” lithospheric deformation associated with the regional extension that has been occurring since late Mesozoic and Cenozoic time. NE China was an elevated terrane after the closure of the Mongol–Okhotsk ocean due to either the continent–continent collision in the west or flat subduction of the Paleo-Pacific plate in the east before the Cretaceous (e.g., Wang et al., 2006; Zhang et al., 2010). Modern orogenies usually show strike-parallel fast polarization directions, perpendicular to the collision-induced compressional directions. For example, McNamara et al. (1994) found that there is a close correlation between the orientation of the large-scale sur-

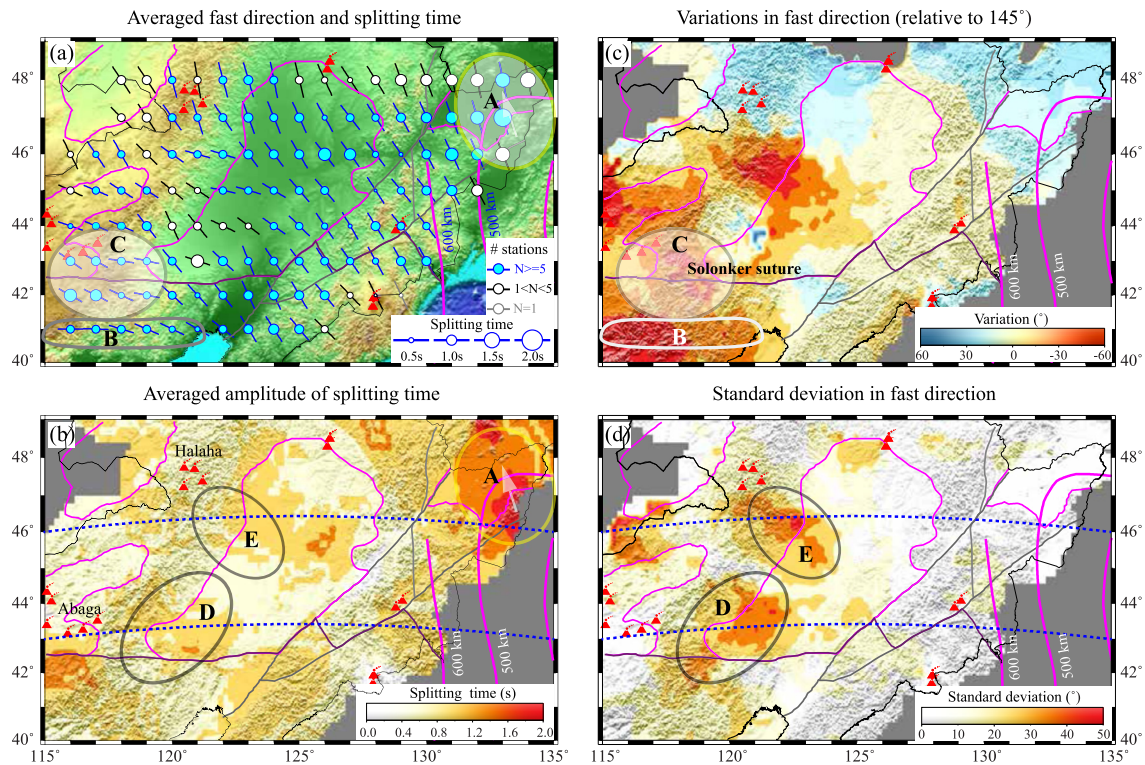


**Fig. 7.** (a) Average fast direction and splitting time using circular caps with a radius of a  $1^\circ$  are plotted on each  $1^\circ \times 1^\circ$  grid in a similar way as Fig. 6a. (b) Color contour map shows the lateral variation of the average splitting time. (c) Deviations of the observed fast polarization direction from the NW–SE direction. (d) Standard deviation in fast direction within each  $1^\circ$  circular cap. Shaded areas marked with the letters A–E are the anomalous regions discussed in the main text. The two dotted blue lines shown in (b) and (d) indicate the geographic locations of the two depth sections of the NECESS P velocity model shown in Fig. 8. Purple lines indicate the Wadati–Benioff zone, showing the geographic location of the subducting Pacific slab at 500 km and 600 km depths. (For interpretation of the references to color in this figure legend, the reader is referred to the web version of this article.)

face deformation and the fast polarization direction from a linear seismic array deployed on the Tibetan plateau. Masy et al. (2011) measured the SKS/SKKS splitting recorded by a broadband array in western Venezuela and found that the Merida Andes exhibits a NE–SW fast direction, which is parallel to trend of the orogen. Both observations are attributed to a vertical coherent deformation within the lithosphere. If the Jurassic deformation associated with the collision after the closure of the Mongol–Okhotsk ocean was frozen and prevalent, then we would expect the shear waves to have a NNE–SSW fast polarization in the area, especially within the Great Xing’an range, which is not observed here. Thus we speculate that thickening related lithospheric deformation might have not been so significant, which implies that lithosphere delamination beneath the Songliao basin, if it had ever occurred, is likely triggered by the flat-to-normal subduction change of the Pacific plate (Zhang et al., 2010).

At around 150–140 Ma, the plateau started to collapse, probably being facilitated by lithosphere delamination, followed by an active period of rifting in the Cretaceous and Cenozoic, which led to the development of the Songliao basin. The delamination could be caused by a negative buoyancy of the thickened lower crust and mantle lithosphere (Wang et al., 2006) or triggered by a change in subduction style from flat to normal (Zhang et al., 2010). The NW–SE rifting initiated in the Cretaceous, which is likely strengthened by the eastward retreat of Pacific subduction in the east, has generated strong extensional deformation in the lithosphere that seems to be the dominant fabric structure of the area. Thus, the observed seismic anisotropy through a large part of NE China seems to reflect this extensional deformation in the lithosphere.

Several stations located in the northeast corner of the study area (area A in Figs. 7a and 6a) exhibit large splitting times

(~1.5 s) and NNW–SSE fast polarization directions, slightly deviated from the general NW–SE trend (Figs. 6a and 7c). Li and Niu (2010) also observed this feature and speculated that it is related to the geometry of the subducting Pacific plate. The deep Wadati–Benioff zone shows that the subducted Pacific plate at 400–600 km depths (purple lines in Fig. 7a) has a clear bend beneath the NE corner of our study area. Recent tomographic images (e.g., Obayashi et al., 2011) found that the high velocity slab is absent at this corner, suggesting a disconnection between the westward and northward dipping segments, which means a possible slab tear at the corner. According to Russo and Silver (1994), a trench parallel flow can form in the mantle behind the slab when a subducting slab rolls back. The presence of slab tear allows the mantle flow to escape, forming a northwest-going flow in our case, which may largely contribute the observed seismic anisotropy.

The measurements in the bottom left corner (area B in Fig. 7a) are from Li and Niu (2010), which show a nearly E–W fast direction (Figs. 6a). These stations are located at the Jurassic Yanshan fold and thrust belt in the North China craton. The E–W fast direction is roughly parallel to the strike of the Yanshan orogenic belt, which was formed due to the collision of the NE China and the North China craton after the closure of the Paleo-Asian Ocean. Thus the observed E–W oriented seismic anisotropy is consistent with fabric structure in the lithosphere due to the N–S directed collision. The E–W oriented structure can be also influenced by a second collision between the NE China and the Siberia craton along the NW–SE direction. This might explain the ENE–WSW fast polarization direction observed by the stations on the southern Great Xing’an range, as well as those across the Solonker suture (area C in Fig. 7a).

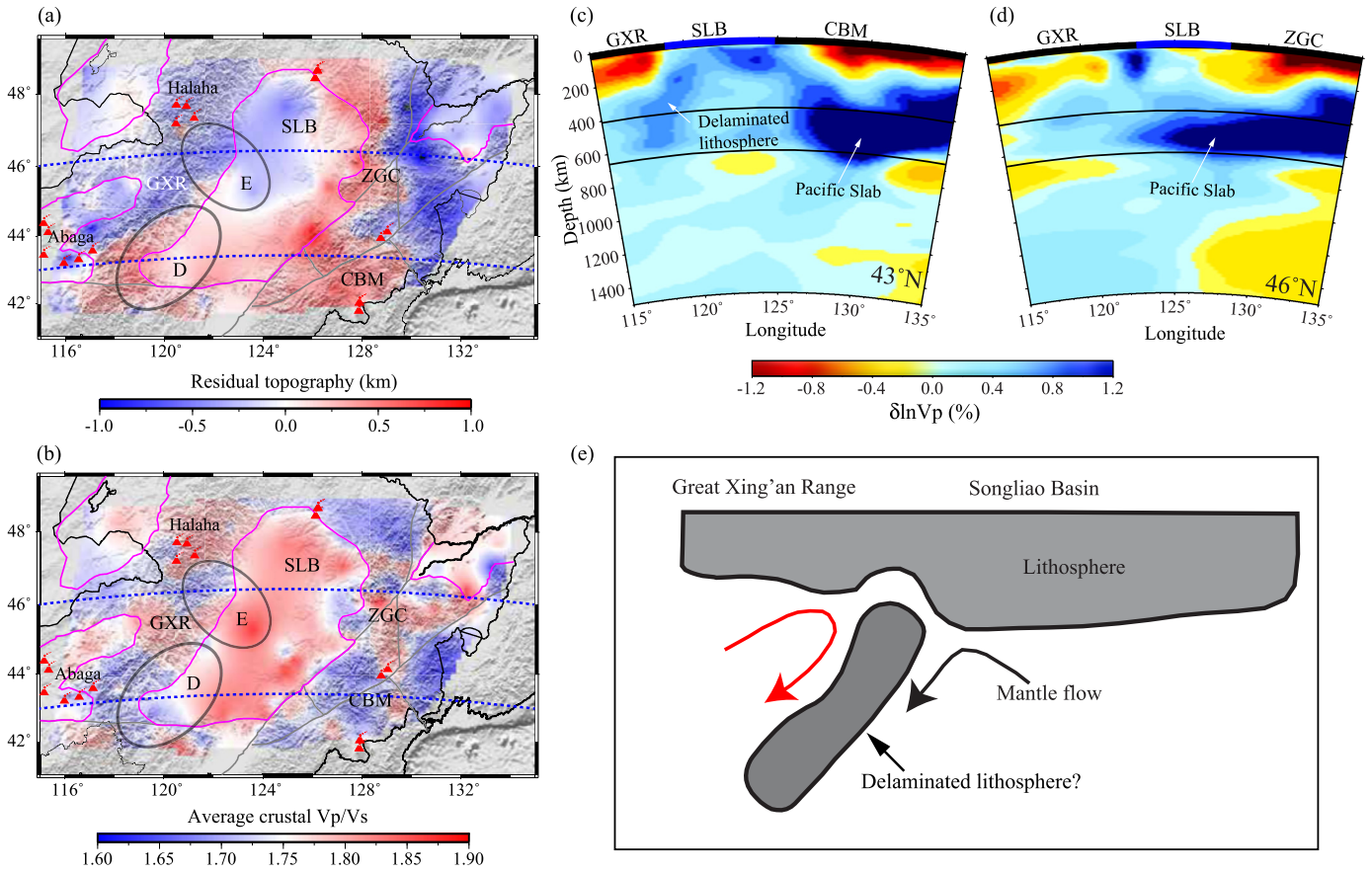


**Fig. 8.** Maps showing residual topography (a) and Vp/Vs ratio (b) that were estimated from receiver function data by Tao et al. (2014). Two depth cross-sections of the 3-D NECESS P velocity model are shown in (c) and (d), which are roughly along the latitudes of 43°N and 46°N, respectively. (e) A schematic diagram showing the ongoing lithospheric delamination beneath the southern Great Xing’an range and southwest Songliao basin. (For interpretation of the references to color in this figure, the reader is referred to the web version of this article.)

3.3. Scenario for a ongoing lithospheric delamination beneath the southern Great Xing’an range

The most anomalous area of the observed seismic anisotropy lies at the border between the southern Great Xing’an range and the Songliao basin (area D in Fig. 7d), where both the fast direction and splitting time exhibit large variations. Li and Niu (2010) also found some variations in fast direction at the west edge of the Songliao basin, which they interpreted as due to the influence of possible edge driven sublithospheric flow (Niu, 2005). With more stations in the area, we are able to confine the anomalous region to the southwestern part of the study area, where ongoing lithospheric delamination is likely present. Such a scenario is also suggested by other seismic data.

Surface wave tomography (e.g., Guo et al., 2015; Liu et al., 2017) shows strong low-velocity anomalies in the lower crust beneath the Great Xing’an range and more localized low velocity zones in the uppermost mantle beneath the Abaga and Halaha volcanic complexes located in the southern and northern segments of the range. Moderately slow anomalies also exist in the lower crust and uppermost mantle beneath the southwestern part of the Songliao basin. A receiver function study (Tao et al., 2014) shows that the crust beneath the southern end of the Great Xing’an range and southwestern Songliao basin is relatively thin with respect to their elevations, indicating that part of the surface topography is dynamically supported by the upper mantle (Fig. 8a). Both observations suggest that a hot and buoyant mantle upwelling might be present beneath the southern Great Xing’an range. We further argue that such a mantle upwelling is induced by an ongoing

lithospheric delamination, which together with the induced return flows, are the likely cause of the observed large variations in seismic anisotropy.

The strongest evidence for potential ongoing lithosphere delamination beneath the southern Great Xing’an range comes from the P-wave tomography (hereafter 3-D NECESS P velocity model, Obayashi et al., 2011). Fig. 8c shows a depth section of the 3-D model along the latitude of 43°N, where a westward dipping high-velocity anomaly can be clearly seen at depths between ~150 and ~600 km. A moderately thick lithosphere is observed here beneath the Songliao basin while the Changbaishan mountain range and the Great Xing’an range are underlain by slow seismic structures at the same depth range. Tang et al. (2014) showed a deep mantle upwelling beneath the Changbaishan volcano, which probably eroded away a large portion of the lithosphere beneath the mountain range. The cold lithosphere beneath the Great Xing’an range was probably replaced by hot asthenosphere due to lithosphere delamination (Figs. 8c and 8e). The lower crust and mantle lithosphere appear to have detached from the upper crust due to negative buoyancy and are sinking into the deep mantle. The involvement of the lower crust in the delamination is signaled by the low averaged crustal Vp/Vs ratio beneath the delaminated area, as indicated by receiver function data (Fig. 8b, Tao et al., 2014), which suggests the crust in the area has a felsic composition (e.g., Kay and Kay, 1993).

The return flow in front of the delaminated lithosphere (red arrow in Fig. 8e) brings up hot asthenospheric material to the uppermost mantle, resulting in the widespread Quaternary volcanism in the area. The late Quaternary Abaga volcanic group

comprises more than 300 volcanoes and a lava plateau spreading over an area of more than 10,000 km<sup>2</sup> (Wang et al., 2006; Chen et al., 2015; Fan et al., 2015). Geochemical studies of the Cenozoic magmatism (e.g., Zou et al., 2008; Chen et al., 2015; Guo et al., 2016) showed that the intraplate alkaline basalts have isotopic signatures close to those of the present-day ocean island basalts (OIBs), which suggests that they have a deep origin in the asthenosphere.

The delamination together with the induced mantle flows (Fig. 8e), on the other hand, also causes the realignment of olivine fabrics, resulting in a complicated anisotropic structure beneath the southern Great Xing'an range and southwest Songliao basin (area D), which are reflected by the observed large variations in fast polarization direction and splitting time.

There is another anomalous region near the central border between the Songliao basin and the Great Xing'an range, ~200 km southeast of the Halaha volcanic complex (area E in Fig. 7d). The complex consists of tens of Quaternary volcanoes that overlie Jurassic intrusive rocks with a peak age of 135–144 Ma (Wang et al., 2006; Fan et al., 2015). Several geochemistry studies (e.g., Guo et al., 2009; Zhang et al., 2010) suggest that the northern and southern Great Xing'an range might have undergone different deep lithospheric processes, as shown in rock assemblages, geochemistry and age of the volcanic rocks. Based on these observations, Zhang et al. (2010) concluded that only the northern Great Xing'an range experienced large-scale lithospheric delamination during the early Cretaceous.

Compared to the southern Great Xing'an range the seismic evidence for a lithospheric delamination in this area is less strong. The P-wave tomographic images shows some suggestive evidence for a delaminated lithosphere below ~200 km under the Great Xing'an range (Fig. 8d). The return flow seems to be much weaker and only shows a slightly positive topographic residual near the Halaha volcanic complex (Fig. 8a). Both observations imply a much smaller scale and/or an older delamination as compared to the south. Therefore, the complexity of seismic anisotropy observed in area E might have been caused by different mechanisms. It could reflect either a present-day deformation caused by a small-scale delamination, or a frozen structure associated with the Cretaceous delamination event.

#### 4. Conclusions

We measured shear wave splitting of SKS/SKKS from 32 earthquakes recorded at 125 stations in NE China with a multi-event stacking method. For stations with multi-azimuth SKS/SKKS data, we did not find obvious azimuthal variations of the splitting parameters. We thus employed a one-layer anisotropic model to fit the shear wave splitting. In general, the measured seismic anisotropy shows a well-organized pattern over the study area. Most stations exhibit an NW–SE fast polarization direction that reflects the extensional deformation associated with the rifting, which has been predominant in the area since the early Cretaceous. We also found a dozen stations located above a lateral bend of the Pacific slab in the northeast corner of the study area possess anomalously high splitting times with a NNW–SSE fast polarization direction. We speculate that the observed seismic anisotropy is likely caused by a sublithospheric flow along a slab tear at the bend as the Pacific slab rolls back toward the east. The most complicated anisotropic structure is observed beneath the southern Great Xing'an range and the southwest Songliao basin. This anisotropic complexity, together with other seismic observations, argues for a scenario of an ongoing large-scale lithospheric delamination beneath the area.

#### Acknowledgements

We thank all the people in the NECESSArray project for installing and servicing the seismic array, Dr. Zhouchuan Huang and another anonymous reviewer for their constructive comments and suggestions, which significantly improved the quality of this paper. F.N. and H.C. were supported by NSF EAR-0635666 and NSFC41274099. S.G. was supported by NSF EAR-0635855, H.K., S.T., and M.O. were supported by the JSPS grant 19104011. Y.C. and J.N. were supported by NSFC grants 40821062 and 90814002.

#### Appendix A. Supplementary material

Supplementary material related to this article can be found online at <http://dx.doi.org/10.1016/j.epsl.2017.04.030>.

#### References

- Becker, T.W., 2008. Azimuthal seismic anisotropy constrains net rotation of the lithosphere. *Geophys. Res. Lett.* 35, L05303. <http://dx.doi.org/10.1029/2007GL032928>.
- Chen, S.S., Fan, Q.C., Zou, H.B., Zhao, Y.W., Shi, R.D., 2015. Geochemical and Sr–Nd isotopic constraints on the petrogenesis of late Cenozoic basalts from the Abaga area, Inner Mongolia, eastern China. *J. Volcanol. Geotherm. Res.* 305, 30–44. <http://dx.doi.org/10.1016/j.jvolgeores.2015.09.018>.
- Crampin, S., 1987. Geological and industrial implications of extensive dilatancy anisotropy. *Nature* 328, 491–496.
- Fan, Q., Zhao, Y., Chen, S., Li, N., Sui, J., 2015. Quaternary volcanic activities in the West of Daxing'anling-Taihangshan gravity lineament. *Bull. Mineral. Petrol. Geochem.* 4, 674–681. <http://dx.doi.org/10.3969/j.issn.1007-2802.2015.04.001> (in Chinese with English abstract).
- Gripp, A.E., Gordon, R.G., 2002. Young tracks of hotspots and current plate velocities. *Geophys. J. Int.* 150, 321–361. <http://dx.doi.org/10.1046/j.1365-246X.2002.01627.x>.
- Guo, F., Fan, W.M., Li, C.W., Gao, X.F., Miao, L.C., 2009. Early Cretaceous highly positive  $\epsilon_{Nd}$  felsic volcanic rocks from the Hinggan Mountains, NE China: origin and implications for Phanerozoic crustal growth. *Int. J. Earth Sci.* 98, 1395–1411. <http://dx.doi.org/10.1007/s00531-008-0362-8>.
- Guo, P., Niu, Y., Sun, P., Ye, L., Liu, J., Zhang, Y., Feng, Y., Zhao, J., 2016. The origin of Cenozoic basalts from central Inner Mongolia, East China: the consequence of recent mantle metasomatism genetically associated with seismically observed paleo-Pacific slab in the mantle transition zone. *Lithos* 240–243, 104–118. <http://dx.doi.org/10.1016/j.lithos.2015.11.010>.
- Guo, Z., Chen, Y.J., Ning, J., Feng, Y., Grand, S.P., Niu, F., Kawakatsu, H., Tanaka, S., Obayashi, M., Ni, J., 2015. High resolution 3-D crustal structure beneath NE China from joint inversion of ambient noise and receiver functions using NECESSArray data. *Earth Planet. Sci. Lett.* 416, 1–11. <http://dx.doi.org/10.1016/j.epsl.2015.01.044>.
- Kay, R.W., Kay, S.M., 1993. Delamination and delamination magmatism. *Tectonophysics* 219, 177–189.
- Kreemer, C., 2009. Absolute plate motions constrained by shear-wave-splitting orientations with implications for hot spot motions and mantle flow. *J. Geophys. Res.* 114, B10405. <http://dx.doi.org/10.1029/2009JB006416>.
- Lei, J., Zhao, D., 2005. P-wave tomography and origin of the Changbai intraplate volcano in Northeast Asia. *Tectonophysics* 397, 281–295. <http://dx.doi.org/10.1016/j.tecto.2004.12.009>.
- Li, J., Niu, F., 2010. Seismic anisotropy and mantle flow beneath northeast China inferred from regional seismic networks. *J. Geophys. Res.* 115, B12327. <http://dx.doi.org/10.1029/2010JB007470>.
- Liu, J., Han, J., Fyfe, W.S., 2001. Cenozoic episodic volcanism and continental rifting in northeast China and possible link to Japan Sea development as revealed from K–Ar geochronology. *Tectonophysics* 339, 385–401. [http://dx.doi.org/10.1016/S0040-1951\(01\)00132-9](http://dx.doi.org/10.1016/S0040-1951(01)00132-9).
- Liu, Y., Niu, F., Chen, M., Yang, W., 2017. 3-D crustal and uppermost mantle structure beneath NE China revealed by ambient noise adjoint tomography. *Earth Planet. Sci. Lett.* 461, 20–29.
- Mainprice, D., Barruol, G., Ismail, B., 2000. The anisotropy of the Earth's mantle: from single crystal to polycrystal. In: Karato, S.-I., Stixrude, L., Liebermann, R., Master, G., Forte, A. (Eds.), *Mineral Physics and Seismic Tomography from the Atomic to the Global Scale*. In: *Geophys. Monogr.*, vol. 117. American Geophysical Union, Washington, DC, pp. 237–264.
- Masy, J., Niu, F., Levander, A., Schmitz, M., 2011. Mantle flow beneath northwestern Venezuela: seismic evidence for a deep origin of the Mérida Andes. *Earth Planet. Sci. Lett.* 305 (3–4), 396–404. <http://dx.doi.org/10.1016/j.epsl.2011.03.024>.
- McNamara, D.E., Owens, T.J., Silver, P.G., Wu, F.T., 1994. Shear wave anisotropy beneath the Tibetan Plateau. *J. Geophys. Res.* 99, 13655–13665.
- Morgan, W.J., 1972. Plate motions and deep mantle convection. *Mem. Geol. Soc. Amer.* 132, 7–22.

- Niu, F., Li, J., 2011. Component azimuths of the CEArray stations estimated from P-wave particle motion. *Earthq. Sci.* 24, 3–13.
- Niu, Y., 2005. Generation and evolution of basaltic magmas: some basic concepts and a new view on the origin of Mesozoic–Cenozoic basaltic volcanism in eastern China. *Geol. J. China Univ.* 11, 9–46.
- Obayashi, M., Kawakatsu, H., Tanaka, S., Chen, Y.J., Ning, J., Grand, S.P., Niu, F., Miyakawa, K., Idehara, K., Tonegawa, T., Iritani, R., 2011. P-wave tomography of Northeastern China observed with NECESSArray. In: Fall Meeting, AGU. San Francisco, Calif., 5–9 Dec., Abstract S24B-06.
- Rumpker, G., Silver, P.G., 1998. Apparent shear-wave splitting parameters in the presence of vertically varying anisotropy. *Geophys. J. Int.* 135, 790–800.
- Russo, R.M., Silver, P.G., 1994. Trench-parallel follow beneath the Nazca plate from seismic anisotropy. *Science* 263, 1105–1111.
- Silver, P.G., 1996. Seismic anisotropy beneath the continents: probing the depths of geology. *Annu. Rev. Earth Planet. Sci.* 24, 385–432.
- Silver, P.G., Chan, W., 1988. Implications for continental structure and evolution from seismic anisotropy. *Nature* 335, 34–39.
- Silver, P.G., Chan, W.W., 1991. Shear wave splitting and subcontinental mantle deformation. *J. Geophys. Res.* 96, 16,429–16,454. <http://dx.doi.org/10.1029/91JB00899>.
- Tang, Y., Obayashi, M., Niu, F., Grand, S.P., Chen, Y.J., Kawakatsu, H., Tanaka, S., Ning, J., Ni, J.F., 2014. Changbaishan volcanism in northeast China linked to subduction-induced mantle upwelling. *Nat. Geosci.* 7, 470–475. <http://dx.doi.org/10.1038/ngeo2166>.
- Tao, K., Niu, F., Ning, J., Chen, Y.J., Grand, S., Kawakatsu, H., Tanaka, S., Obayashi, M., Ni, J., 2014. Crustal structure beneath NE China imaged by NECESSArray receiver function data. *Earth Planet. Sci. Lett.* 398, 48–57. <http://dx.doi.org/10.1016/j.epsl.2014.04.043>.
- Wang, F., Zhou, X., Zhang, L., Ying, J., Zhang, Y., Wu, F., Zhu, R., 2006. Late Mesozoic volcanism in the Great Xing'an Range (NE China): timing and implications for the dynamic setting of NE Asia. *Earth Planet. Sci. Lett.* 251, 179–198. <http://dx.doi.org/10.1016/j.epsl.2006.09.007>.
- Wustefeld, A., Bokelmann, G., 2007. Null detection in shear-wave splitting measurements. *Bull. Seismol. Soc. Am.* 97, 1204–1211.
- Xu, Y., Zhang, H., Qiu, H., Ge, W., Wu, F., 2012. Oceanic crust components in continental basalts from Shuangliao, Northeast China: derived from the mantle transition zone? *Chem. Geol.* 328, 168–184.
- Zhang, J., Gao, S., Ge, W., Wu, F., Yang, J., Wilde, S.A., Li, M., 2010. Geochronology of the Mesozoic volcanic rocks in the Great Xing'an Range, northeastern China: implications for subduction-induced delamination. *Chem. Geol.* 276, 144–165.
- Zheng, L., Gordon, R.G., Kreemer, C., 2014. Absolute plate velocities from seismic anisotropy: importance of correlated errors. *J. Geophys. Res.* 119, 7336–7352. <http://dx.doi.org/10.1002/2013JB010902>.
- Zheng, X., Ouyang, B., Zhang, D., Yao, Z., Liang, J., Zheng, J., 2009. Technical system construction of Data Backup Centre for China Seismograph Network and the data support to researches on the Wenchuan earthquake. *Chin. J. Geophys.* 52, 1412–1417. <http://dx.doi.org/10.3969/j.issn.0001-5733> (in Chinese).
- Zou, H., Fan, Q., Yao, Y., 2008. U-Th systematics of dispersed young volcanoes in NE China: asthenosphere upwelling caused by piling up and upward thickening of stagnant Pacific slab. *Chem. Geol.* 255, 134–142. <http://dx.doi.org/10.1016/j.chemgeo.2008.06.022>.